RSC Advances

PAPER

Arsine adsorption in copper-exchanged zeolite under low temperature and micro-oxygen conditions

Xueqian Wang, Yingjie Zhang, Ping Ning, [ID] * Shudi Yan, Langlang Wang and Qiang Ma

Arsenic pollution is a worldwide issue. Nearly all arsenic is converted to arsine (AsH_3) under the reducing atmosphere required for the gasification process. Growing industrialization has increased AsH_3 emissions, for example, the ore smelting process leads to AsH_3 emissions. The conditions used in the ore smelting process are low temperature and micro-oxygen. A series of Hβ zeolites loaded on different metal oxides has been prepared using an impregnation method and tested for adsorption of arsine (AsH_3) under low temperature and micro-oxygen conditions. Based on the results obtained from the adsorbent optimization experiments, Hβ zeolite modified with $Cu(NO_3)_2$ (denoted as Cu/Hβ) was found to possess a significantly enhanced adsorption removal ability towards arsine. The effects of the impregnation concentration, calcination temperature, reaction temperature, and oxygen content on the AsH_3 removal process were investigated. The results indicate that adsorbents with $0.2\ mol\ L^{-1}\ Cu(NO_3)_2$ after calcination at 400 °C have superior activity for AsH_3 removal. In addition, a breakthrough capacity of 43.7 mg AsH_3/g adsorbent at 60 °C as well as 1.0% oxygen was observed with Cu/Hβ for the AsH_3 adsorption process. The structure and surface properties of the Hβ zeolite samples were characterized by N_2-BET (N_2 adsorption/desorption), XRD (X-ray powder diffraction), XPS (X-ray photoelectron spectroscopy), and FTIR (Fourier transform infrared) spectroscopy. It is feasible that the exhausted Cu/Hβ can be regenerated by thermal desorption, and the adsorbents can be recycled at least two times with little capacity loss.

1. Introduction

Arsine (AsH_3) is a hydrophobic, very volatile, and highly poisonous gas, which plays an important role in the cycling of arsenic on earth. AsH_3 released in the air commonly arises from various sources such as the processes in which arsenic-containing metals react with acids, coal gasification, yellow phosphorus tail gas, and the burning of fossil fuels at high temperatures.[1-6] For example, ore smelting flue gas includes reducing gaseous pollutants such as AsH_3 and H_2S; however, arsenic emissions during the ore smelting process have not received adequate attention due to the micro-oxygen and low temperature conditions used; thus, these emissions have been easily overlooked despite their toxicity.[37] The toxicity of AsH_3 is about seven times higher than that of lewisite.[7] AsH_3 can enter the body through skin, respiratory tract or the digestive tract, which can easily induce severe human health hazards including serious damage to the lungs, respiratory tract, bronchus, and kidneys as well as cancer.[8] Thus, the concentration of AsH_3 in the workshop has been strictly limited in many countries. For instance, the permissible exposure limit of AsH_3 should be

between $0.016\ mg\ m^{-3}$ and $0.001\ mg\ m^{-3}$, which has been defined by the American Committee of government in Health and the Ministry of Environmental Protection of the People's Republic of China, respectively.[9] Furthermore, synthesis gas can be used to produce C1 chemical products with the development of C1 chemical technology. However, the most important factors of synthesis catalyst poisoning is the existence of many impurities such as sulfur, phosphorus, arsenic, and cyanide in synthesis gas.[10,11] Therefore, the removal of AsH_3 has a profound significance.

In general, the methods for removing AsH_3 from air and off-gas include chemical adsorption, catalytic decomposition, combustion, and adsorption. However, catalytic decomposition and combustion are typically employed at high temperatures. Adsorption is one of the most mature and promising methods because of its ease of operation, flexible design, low temperature condition, and low-cost, and it is more appropriate for the removal of AsH_3 at low concentrations. Adsorption technology was chosen to accomplish the required removal of contaminants. Although numerous materials have been reported as adsorbents for the effective removal of AsH_3, high operating temperatures are typically required.[12-18] For instance, Poulston et al. have reported that Pd can be used to modify Al_2O_3 for the adsorption of AsH_3 from simulated flue gas at temperatures

Faculty of Environmental Science and Engineering, Kunming University of Science and Technology, Kunming 650500, China. E-mail: ningping_58@163.com

between 204 °C and 288 °C.[19] Jiang *et al.* found that activated carbon modified with sulfonated cobalt phthalocyanine (CoPcS) and $Cu(NO_3)_2$ was able to adsorb AsH_3 efficiently, and the AsH_3 adsorption capacity was 35.7 mg g^{-1} adsorbent at 60 °C and a 4% oxygen content.[20] However, some shortcomings with the present activated carbons have been identified including their thermal instability.[21] On the other hand, zeolite materials have been found to have broad applications in various fields including as a catalyst support as well as in the development of adsorbents due to their stable structures, large specific surface area, well-developed porous structure, and high thermal stability.[22] However, the possibility of removing AsH_3 using zeolite dry adsorption has not been studied to date. Thus, Hβ zeolite was chosen as the adsorbent support in this study.

The objective of this study was to investigate the adsorption behavior of the modified zeolite adsorbents under low temperature and micro-oxygen conditions and to explore the adsorption mechanism of AsH_3 adsorption removal. Herein, the adsorbents were prepared using an impregnation method, and the effects of the experimental conditions, including the types of impregnant, impregnation concentration, calcination temperature, reaction temperature, and oxygen content, were explored; this allowed us to obtain the optimal adsorption purification conditions for AsH_3. The pore structure properties of the Cu/Hβ zeolite adsorbents before and after AsH_3 adsorption were measured using N_2-BET analysis. The phase and crystalline orientation of Cu/Hβ were determined using XRD analysis. XPS was employed to evaluate the chemical states of the elements in Cu/Hβ before and after AsH_3 adsorption. Functional group and chemical bonding in the Cu/Hβ adsorbents were determined using FTIR spectroscopy.

2. Materials and methods

2.1 Sample preparation

Hβ zeolite prepared from the commercial zeolite (99.99%, Nankai University Catalyst Co., Ltd., Tianjin, China) was used as a support material for metal adsorbents in our experiments. $Cu(NO_3)_2$, $Fe(NO_3)_3 \cdot 9H_2O$, $Zn(NO_3)_2 \cdot 6H_2O$, $Ni(NO_3)_2 \cdot 6H_2O$, $Mn(NO_3)_2$, and $Pb(Ac)_2 \cdot 3H_2O$ were used as impregnates to improve the adsorption performance of the Hβ zeolite. M–Hβ (M = metal) zeolites were prepared using an impregnation method. At first, the Hβ zeolite was crushed and sieved with a 40–60 mesh size. The Hβ zeolite support (10 ± 0.1 g) was washed three times with 150 mL of distilled water at 70 °C to remove the soluble impurities and then dried at 110 °C for 12 h. Subsequently, the Hβ zeolite was impregnated with an aqueous $Cu(NO_3)_2$ solution (0.2 mol L^{-1}, 50 mL), an aqueous $Fe(NO_3)_3$·$9H_2O$ solution (0.2 mol L^{-1}, 50 mL), an aqueous $Zn(NO_3)_2$·$6H_2O$ solution (0.2 mol L^{-1}, 50 mL), an aqueous $Ni(NO_3)_2 \cdot 6H_2O$ solution (0.2 mol L^{-1}, 50 mL), an aqueous $Mn(NO_3)_2$ solution (0.2 mol L^{-1}, 50 mL) or an aqueous $Pb(NO_3)_2$ solution (0.2 mol L^{-1}, 50 mL) at ambient temperature. Then, impregnation was carried out under stirring for 24 h, and the adsorbent was filtered from the reaction solution. The filtered adsorbent was dried at 110 °C for 12 h followed by calcination in a muffle furnace at a specified temperature for 6 h. Finally, the

resulting samples were cooled down to ambient temperature and denoted as Cu/Hβ, Fe/Hβ, Zn/Hβ, Ni/Hβ, Mn/Hβ, and Pb/Hβ.

2.2 Fixed-bed adsorption experiment

The model gas was composed of nitrogen with 70 ppm AsH_3, which was mixed in the mixer evenly with micro-oxygen and subsequently introduced into the adsorption bed unit. This adsorption reaction was conducted in a quartz columnar reactor with a 9 mm inner diameter and 60 mm length under atmospheric pressure. The AsH_3 breakthrough curves for AsH_3 removal were assessed using dynamic tests at temperatures between 20 and 80 °C with an oxygen content between 0% and 2%. Each sample (0.4 g) was added to the quartz column and exposed to the gas containing 70 ppm AsH_3 at a flow rate of 200 mL min^{-1}, and the experiment was stopped when the adsorbent was saturated. AsH_3 was adsorbed readily in potassium permanganate to avoid any safety problems. The concentration of AsH_3 was measured using a silver diethyldithiocarbamate spectrophotometric method. The breakthrough time was defined as the time at which the AsH_3 outlet concentration reached 5% of the inlet concentration according to the breakthrough curves. The adsorption capacity of AsH_3 was calculated with the corresponding integral according to the following equation under various conditions of the breakthrough curves.[23]

$$X = \left(QC_0 t - Q \int_0^t C \mathrm{d}t \right) \Big/ m$$

where X is the adsorption capacity in mg g^{-1}, Q denotes the gas flow rate in m^3 min^{-1}, t represents the adsorption time in minutes, C_0 represents the adsorption column entrance mass concentration of AsH_3 in mg m^{-3}, C represents the adsorption column outlet mass concentration of AsH_3 in mg m^{-3}, and m is the mass of adsorption in g obtained from the breakthrough curves.

2.3 Sample characterization

The pore size distribution, specific surface area, and pore volume of the samples were measured using the nitrogen adsorption/desorption isotherms obtained at 77 K using a NOVA 2000e (Quanta chrome instruments) surface area analyzer. The specific surface area was determined using the Brunauer–Emmett–Teller (BET) equation. The pore size distribution was evaluated using the Barrett–Joyner–Halenda (BJH) method. X-ray diffraction (XRD) patterns were obtained using a Rigaku diffractometer (D/MAX-2200), which was operated under the conditions of 36 kV and 30 mA using Ni-filtered Cu-Kα radiation ($\lambda = 0.15406$ nm) at a rate of 5° min^{-1} from $2\theta = 5$–80°. X-ray photoelectron spectroscopy (XPS) was carried out using an ESCALAB 250 spectrometer, in which the X-ray source was operated with an Al-Kα radiation source with a photoenergy of $h\nu = 1361$ eV. The core-level binding energy of the C 1s peak (284.8 eV) was used for calibration. Fourier transform infrared (FTIR) spectroscopy spectra were obtained using the

KBR pellet technique *via* a Thermo spectrometer in the wave-number range between 4000 and 300 cm^{-1}.

3.   Results and discussion

3.1   Characterization of the samples

3.1.1   N$_2$-BET analysis. The structural parameters of the Hβ zeolite, Cu/Hβ, and Cu/Hβ–AsH$_3$ (Cu/Hβ after the adsorption of AsH$_3$ and the same expression corresponding to the corresponding meaning) were obtained from the nitrogen adsorption/desorption experiments, and the results are shown in Fig. 1. The pore size distribution curves are plotted in Fig. 2. The BET surface area, micro- and total-pore volume, and average pore radius of the samples are summarized in Table 1.

According to the IUPAC classification,[26] the nitrogen adsorption–desorption isotherms of all the samples studied belong to the IUPAC type IV classification, suggesting that the adsorbents are mesoporous materials, and the capillary condensation phenomenon may occur in their pore channels. As illustrated in Fig. 1, the N$_2$ adsorption capacity of the plain Hβ zeolite seems to be greater than that of the Cu/Hβ and Cu/Hβ–AsH$_3$ samples; this is probably because the pores of Cu/Hβ and Cu/Hβ–AsH$_3$ are partially covered by the active ingredient, and the surface area reduces. Furthermore, the hysteresis loop shifts in the relative pressure range of 0.4–1.0, which is a typical characteristic of mesoporous structures. It is considered that the position of the inflection point of P/P_0 relates to a diameter in the mesoporous range, and the sharpness of the step shows the uniformity of the mesoporous size distribution.

The pore size distribution curves in Fig. 2 show that all the samples have pores in the radius range of 1.5–4.5 nm; this further confirms that all the samples are mesoporous. It can also be observed that the volume of the mesopores decreases in the order of Hβ zeolite > Cu/Hβ > Cu/Hβ–AsH$_3$. This is because the pores are blocked by the active ingredients during the
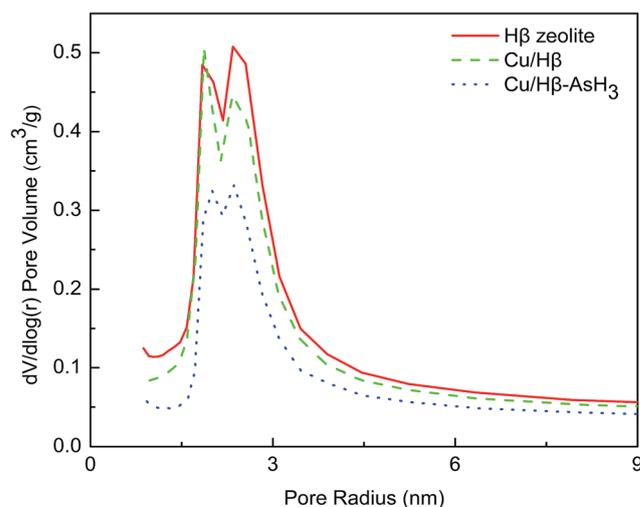

Fig. 2   The pore size distributions of Hβ zeolite and the Cu(NO$_3$)$_2$-modified samples before and after AsH$_3$ adsorption.

impregnation process and the products after the reaction; this ultimately leads to a decrease in the pore volume.

Detailed information on the textural properties of these samples is provided in Table 1. As illustrated in Table 1, when compared with Hβ zeolite, the Cu/Hβ and Cu/Hβ–AsH$_3$ samples show that the impregnation process causes a decrease in the volume of pore radius in the range of 1.5–4.5 nm. The surface areas of the Cu/Hβ and Cu/Hβ–AsH$_3$ samples were found to be 10.8% and 36.8% lower, and the volumes of the samples seemed to decrease by 12.8% and 39.3%, respectively.

As is well known, the presence of a large pore size is considered as fundamental for zeolite materials used in the field of adsorbents. These pore structures can provide more adsorption sites. Moreover, the AsH$_3$ molecules can easily pass through the pore structures and enter the interior of the Hβ zeolite; this is beneficial to improve the amount of AsH$_3$ adsorption on the Hβ zeolite.

3.1.2   XRD analysis. The phase and crystalline orientation of the Hβ zeolite and Cu/Hβ samples with different impregnation concentrations calcined at 400 °C were determined by XRD, as shown in Fig. 3. It can be seen that comparatively weak changes are detected at a lower impregnation concentration (<0.2 mol L^{-1}). This was probably because the concentration of Cu(NO$_3$)$_2$ was very low on the surface of the Hβ zeolite, and the Cu species on the Hβ adsorbent were highly dispersed on the surface of the samples. In addition, Hβ zeolite is non-crystalline and its background peak is obvious, whereas the amount of
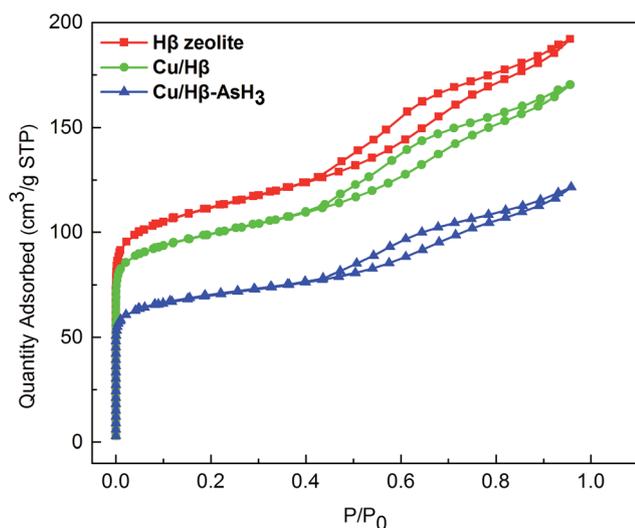

Fig. 1   The nitrogen adsorption/desorption isotherms obtained for Hβ zeolite and the Cu(NO$_3$)$_2$ modified samples before and after AsH$_3$ adsorption.

Table 1   The pore and surface characteristics of Hβ zeolite and the Cu(NO$_3$)$_2$ modified samples before and after AsH$_3$ adsorption

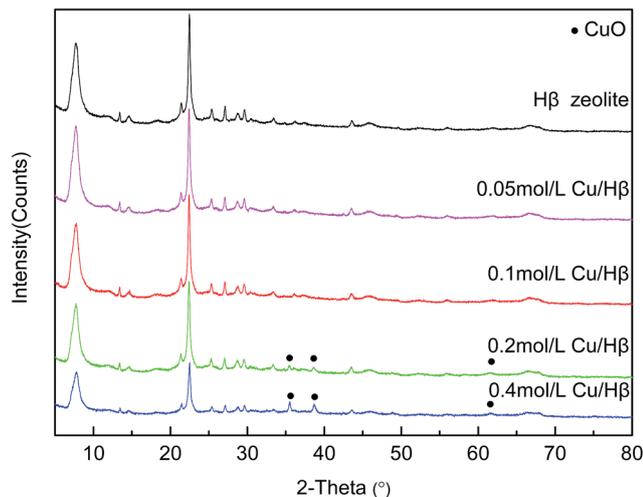| Samples	S_{BET} (m^2 g^{-1})	V_{micro} (cm^3 g^{-1})	V_{total} (cm^3 g^{-1})	$D_{average}$ (nm)
Hβ zeolite	416.6	0.1080	0.2094	2.2322
Cu/Hβ	371.6	0.0993	0.1826	2.2866
Cu/Hβ–AsH$_3$	263.4	0.0730	0.1271	2.4291

Fig. 3 The XRD patterns obtained for the Cu/Hβ zeolites prepared with different impregnation concentrations of Cu^{2+}.

Fig. 4 The XPS spectra obtained for (a) Cu/Hβ and (b) Cu/Hβ–AsH$_3$.

metal oxide is far less than that of zeolite. However, the peaks tend to become more intense upon increasing the impregnation concentration (0.2–0.4 mol L^{-1}). As shown in Fig. 3, peaks with strong intensity appear at $2\theta = 35.4$, 38.7, and 61.5°. These diffraction peaks matched with CuO, which was used as the active component and existed in the Hβ zeolite, and the amount of CuO increased upon increasing the Cu(NO$_3$)$_2$ impregnation concentration from 0.2 to 0.4 mol L^{-1}. Cu(NO$_3$)$_2$, Cu(OH)$_2$, and Cu(CO$_3$)$_2$ can be transformed into CuO under the calcination conditions, and CuO can enhance the adsorption activity. Although the content of CuO is highest at 0.4 mol L^{-1}, the active sites will be occluded by overfull metal oxides, which decrease the adsorption activity. Simultaneously, it can be seen from the Fig. 3 that the characteristic diffraction peaks of the Hβ zeolite with strong intensity appear at $2\theta = 7.7$, 22.5, 25.4, 27.1, 28.7, 29.7, and 43.5°, indicating that the crystal form of the modified Hβ zeolite remains intact. The calcination process also appears to have no effect on the sample pore structure; this indicates that the Hβ zeolite has good thermal stability.

3.1.3 X-ray photoelectron spectroscopic analysis. To ascertain whether the adsorption mechanism was associated with Cu^{2+} and As^{3-}, XPS analysis was employed to examine the composition of the elements Cu and As in the fresh and exhausted adsorbents to determine the valence states of Cu and As on the adsorbent surface. As shown in Fig. 4, a new peak (As 2p) was seen on the Cu/Hβ–AsH$_3$ adsorbents, suggesting that AsH$_3$ was adsorbed on the adsorbents. In addition, in the case of after AsH$_3$ adsorption, the XPS survey spectra exhibited prominent peaks, which included Cu 2p, O 1s, and C 1s, which obviously diminished. These phenomena may result from the involvement of these elements in AsH$_3$ adsorption, thus leading to a change in the intensity of these elemental peaks.

Fig. 5 shows the XPS spectra of the core-level binding energies in Cu 2p (b) before and after the adsorption of AsH$_3$ as well as As 2p (a) after the adsorption of AsH$_3$. The XPS data of the Cu 2p and As 2p spectra and their possible statuses before and after
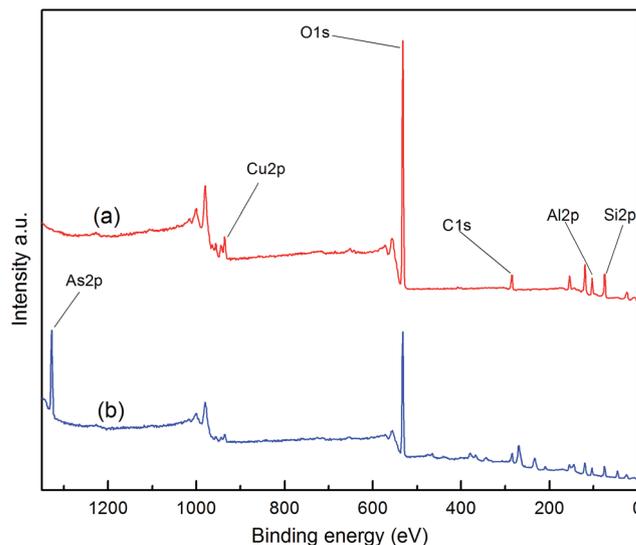
AsH$_3$ adsorption are listed in Table 2. As noted in Fig. 5 and Table 2, the main Cu 2p$_{3/2}$ peak centers are located at 935.5 eV in the presence of a small satellite peak centers located at 943.9 eV and assigned to CuO,[27] which is consistent with the XRD results shown in Fig. 3. In addition, the XPS analysis of As 2p for Cu/Hβ–AsH$_3$ was also conducted to clarify the reaction products. Fig. 5 illustrates that the As 2p peak is centered at 1328.2 eV, indicating the possible presence of As$_2$O$_5$.[28] The As species appearing in Cu/Hβ–AsH$_3$ are likely to be formed via an oxidation process. Freshly prepared Cu/Hβ adsorbent shows no signs of As species, whereas after adsorption, it clearly contains As species.

On the basis of the abovementioned XPS results, it was confirmed that Cu(NO$_3$)$_2$ played a very important role in the AsH$_3$ adsorption process, in which AsH$_3$ seemed to be fixed on the surface of the zeolite. There is no doubt that a higher quantity of As$_2$O$_5$ has been formed on the Cu/Hβ sample when compared with the case of the plain Hβ zeolite. These results suggest that Cu/Hβ may participate in the catalytic oxidation reaction during the process when zeolite adsorbs AsH$_3$.

3.1.4 Infrared spectroscopy analysis. To further understand the changes in the functional groups and chemical bonds of the samples before and after the adsorption of AsH$_3$, FTIR spectroscopy has been carried out. The FTIR spectra of the samples are presented in Fig. 6. It was notable that the peaks at 3438.45, 1632.44, 1382.23, 1228.71, 1095.78, 789.33, 620.58, 568.13, and 464.25 cm^{-1} appeared in the spectra of both the Cu/Hβ and Cu/Hβ–AsH$_3$ samples; this suggested that they possessed similar functional groups or chemical bonds on their surface.

In Fig. 6, we can see a broad strong adsorption band at 3438 cm^{-1}, which can be attributed to the ν(O–H) stretching vibrations of water or phenolic hydroxyl groups associated with hydrogen bonds and carboxylic groups.[29–32] The broad band centered at 1632 cm^{-1} can be assigned to the δOH bending vibration of H$_2$O molecules in the interlayer spaces.[33] The band
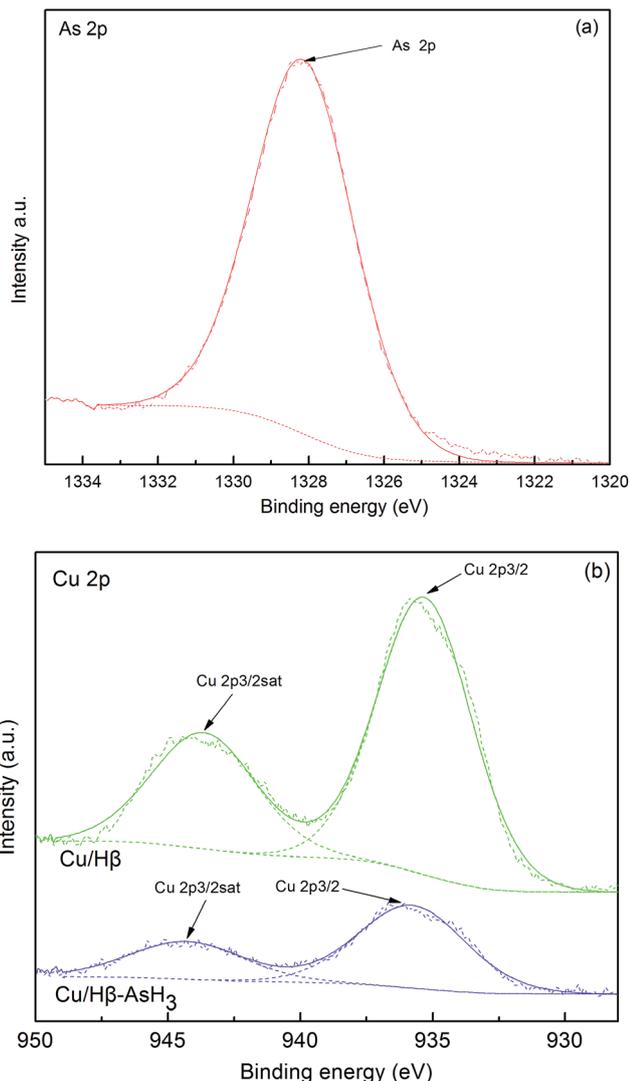
Fig. 5 The XPS spectra obtained for (a) As 2p and (b) Cu 2p.

at around 1382 cm^{-1} was the IR characteristic peak of NO_3^-, which originated from $(Cu(NO_3)_2)$ used in the adsorbent preparation process.[25] It may be inferred that a small amount of nitrate may not decompose during the calcination step performed at 400 °C for 6 h. Another broad peak in the 700–1200 cm^{-1} region with a maximum at about 1095.78 cm^{-1} and a weak shoulder peak appearing at about 1228.71 cm^{-1} can be assigned to C–O vibrations of alcohol groups.[34] The band at
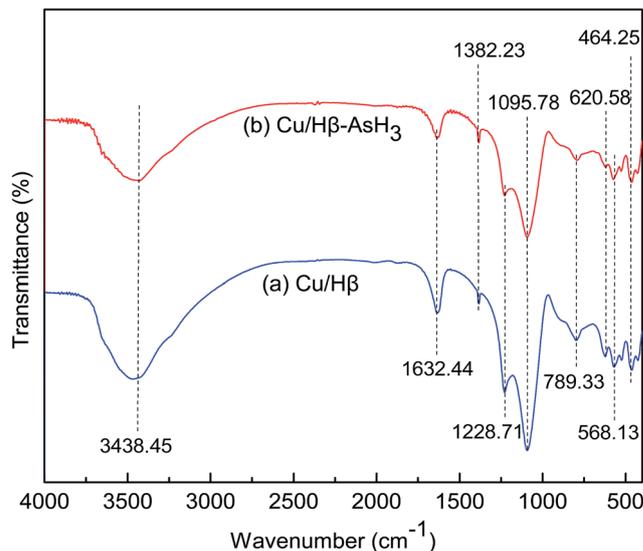

Fig. 6 The FTIR spectra obtained for (a) Cu/Hβ and (b) Cu/Hβ−AsH₃.

620 cm^{-1} was assigned to coupled Al–O and Si–O out-of-plane vibrations.[35] The spectra of the samples have absorption bands characteristic of amorphous silica (790 cm^{-1}), which confirm that the zeolite structure is not decomposed.[35] The bands appearing below 600 cm^{-1} can be assigned to the M–OH and M–O lattice vibration modes,[36] and the peaks observed at 464.25 cm^{-1} and 568.13 cm^{-1} are due to ν(CuO) vibrations.[35] The abovementioned results are consistent with the conclusions obtained from the XRD patterns; the characteristic feature of the zeolite has not been destroyed and CuO is formed at a calcination temperature of 400 °C. The IR spectra of the adsorbents (Cu/Hβ-400 °C, Cu/Hβ-400 °C–AsH₃) are similar; however, in the case after AsH₃ adsorption, the vibrations at 3438.45, 1632.44, and 1228.71 cm^{-1} (corresponding to O–H, δOH, and C–O, respectively) have been obviously diminished. This may be a result of the involvement of these functional groups and chemical bonds in the AsH₃ adsorption process, thus leading to a change in the intensity of these functional groups.

3.2 Performance of the adsorbents

3.2.1 The effects of modifiers on AsH₃ adsorption. Hβ zeolites modified with six metal precursors *via* impregnation were used to investigate the adsorption performance towards AsH₃. Their adsorption capacities were determined and

Table 2 The XPS results of the Cu 2p and As 2p spectra, and their possible statuses before and after AsH₃ adsorption

Element status	Cu/Hβ		Cu/Hβ–AsH₃		
	CuO		CuO		As₂O₅
Binding energy (eV)	Cu 2p$_{3/2}$, 935.31	Cu 2p$_{3/2sat}$, 943.64	Cu 2p$_{3/2}$, 935.74	Cu 2p$_{3/2sat}$, 944.28	As 2p$_{3/2}$, 1328.15
fwhm (eV)	4.198	4.628	4.821	4.932	3.174
Doublet separation (eV)	8.33		8.54		
Calculated As percentage (%)	—	—	—	—	100

compared in dynamic removal capacity tests with AsH$_3$. The breakthrough curves for AsH$_3$ on the abovementioned adsorbents are displayed in Fig. 7. It can be seen that AsH$_3$ has been removal effectively after the adsorption treatment, whereas their breakthrough curves have significant differences in their adsorption performance as AsH$_3$ adsorbents. The breakthrough times of the adsorbents increased in the following sequence: Hβ zeolite < Mn/Hβ < Ni/Hβ < Zn/Hβ < Fe/Hβ <Pb/Hβ < Cu/Hβ. The Cu/Hβ sample showed a significant improvement towards AsH$_3$ adsorption with a breakthrough time of 390 min and a breakthrough capacity of 37.1 mg g^{-1}. The impregnation of Cu(NO$_3$)$_2$ leads to an increase in both the breakthrough time and the amount of AsH$_3$ adsorbed by the Hβ zeolite. It can be deduced that the excellent adsorption performance of the Cu/Hβ adsorbent may be attributed to the active groups formed upon the introduction of Cu(NO$_3$)$_2$,[24] which will add to the physical adsorption sites and lead to a strong chemical adsorption process.

3.2.2 The effects of the Cu^{2+} impregnation concentration on AsH$_3$ adsorption. The impregnation concentration of active components in the process of preparing the adsorbent is one of the most principal factors that affect the removal efficiency in the AsH$_3$ adsorption process. Different concentrations of Cu(NO$_3$)$_2$ solutions ranging from 0.05 to 0.4 mol L^{-1} were used to obtain Cu/Hβ adsorbents with various metal loading amounts. Fig. 8 shows how the Cu^{2+} impregnation concentration affects the AsH$_3$ breakthrough at different impregnation concentrations of 0.05, 0.1, 0.2, and 0.4 mol L^{-1}. It was found in Fig. 8 that the adsorption efficiency of the modified Hβ zeolite was influenced by the concentration of Cu(NO$_3$)$_2$ in the following sequence: 0.2 mol L^{-1} > 0.1 mol L^{-1} > 0.4 mol L^{-1} > 0.05 mol L^{-1} > Hβ zeolite. The corresponding breakthrough capacities were 37.1 mg g^{-1}, 33.3 mg g^{-1}, 27.6 mg g^{-1}, and 22.8 mg g^{-1}, which changed with the impregnation concentration. It can be deduced that a lower concentration of Cu^{2+} cannot provide a sufficient number of active groups, and
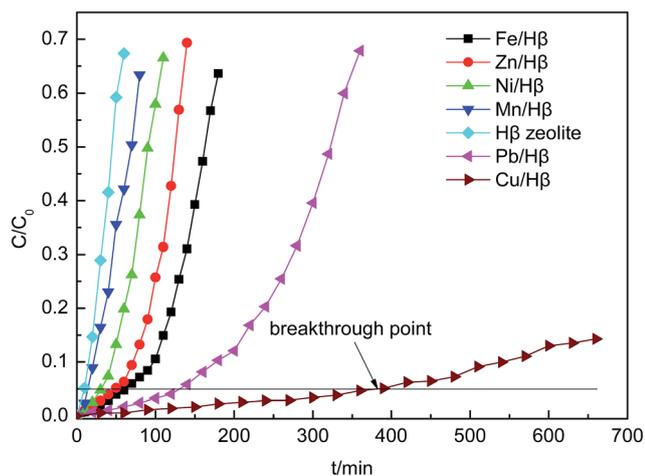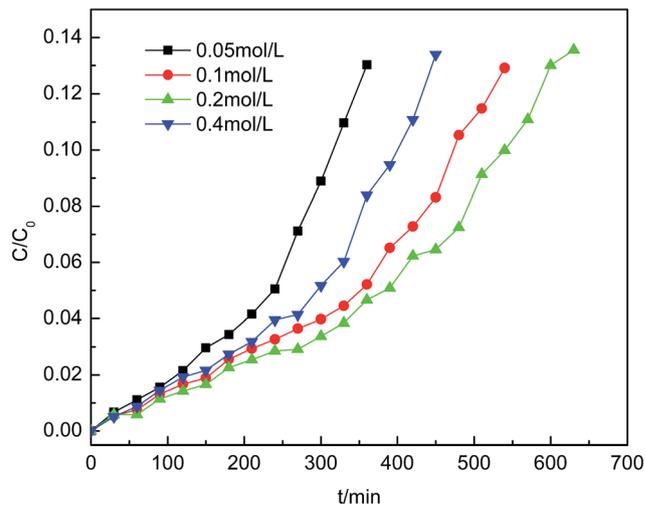

Fig. 8 The AsH$_3$ breakthrough curves obtained for the samples prepared with different concentrations of Cu(NO$_3$)$_2$ loaded on the Hβ zeolite at 60 °C with 1.0% O$_2$ (AsH$_3$ inlet concentration = 200 mg m^{-3} and calcination temperature = 300 °C).

a higher concentration may cause the blockage of the micropores in the adsorbent and a decrease in the specific surface area. Therefore, 0.2 mol L^{-1} was selected as the optimal impregnation concentration for the Cu/Hβ adsorbent preparation process.

To evaluate the performance of the adsorbents, the actual Cu metal loadings of adsorbents were measured using inductively coupled plasma (ICP) analysis. As the impregnation concentration of Cu(NO$_3$)$_2$ was increased from 0.05 to 0.4 mol L^{-1}, the copper element loading amount increased linearly. The sample of copper-exchanged zeolite with better efficiency was impregnated with 0.2 mol L^{-1} Cu^{2+} and had a Cu loading amount of 10.87 wt%.

3.2.3 The effects of the calcination temperature on AsH$_3$ adsorption. The calcination temperature used in the adsorbent preparation process is one of the key factors that can influence the AsH$_3$ removal efficiency and adsorption capacity. It has a great effect on the activation, grain distribution, crystal formation, pore volume, porosity, pore size distribution, and stability of the modified Hβ zeolite. The calcination temperature can influence the decomposition of the metal salts and relates to the redistribution and aggregation of products on the zeolite surface.[25] Fig. 9 shows the AsH$_3$ adsorption breakthrough curves of the Cu/Hβ samples calcined at 200, 300, 400, and 500 °C when the impregnation concentration of Cu(NO$_3$)$_2$ is 0.2 mol L^{-1}. As observed from Fig. 9, a too low or too high calcination temperature is disadvantageous for AsH$_3$ adsorption. The adsorption efficiency at different calcination temperatures increased in the following order: Cu/Hβ-200 °C < Cu/Hβ-500 °C < Cu/Hβ-300 °C < Cu/Hβ-400 °C. Low temperature does not result in enough Cu(NO$_3$)$_2$ decomposition to form a sufficient amount of CuO and further effects the dispersion of CuO on the surface of the zeolite support. In contrast, a high temperature can decompose the active substances and destroy the pore structure, which will finally affect the adsorptive
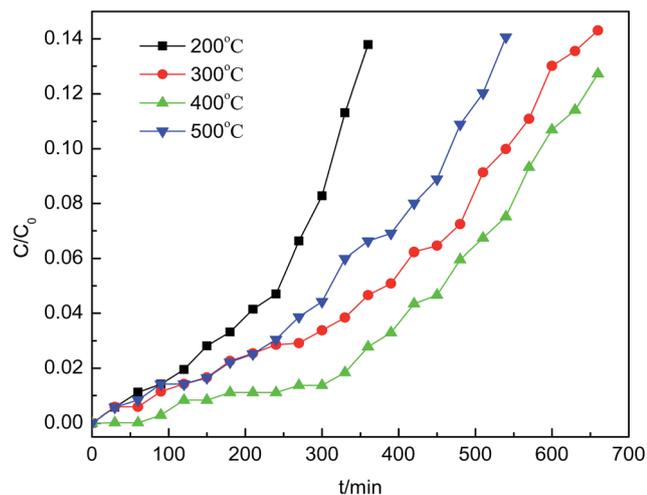

Fig. 7 The AsH$_3$ breakthrough curves obtained for the different adsorbents at 60 °C with 1.0% O$_2$ (AsH$_3$ inlet concentration = 200 mg m^{-3}, calcination temperature = 300 °C and impregnation concentration = 0.2 mol L^{-1}).

Fig. 9 The AsH$_3$ breakthrough curves obtained for the samples prepared at different calcination temperatures at 60 °C with 1.0% O$_2$ (AsH$_3$ inlet concentration = 200 mg m^{-3} and impregnation concentration = 0.2 mol L^{-1}).
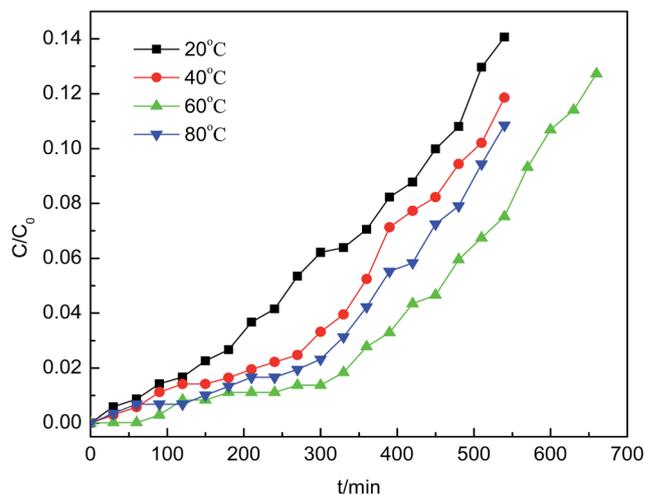

Fig. 10 The AsH$_3$ breakthrough curves obtained for a Cu/Hβ fixed bed as a function of the reaction temperature in the presence of 1.0% O$_2$ (AsH$_3$ inlet concentration = 200 mg m^{-3}, impregnation concentration = 0.2 mol L^{-1} and calcination temperature = 400 °C).

properties of the modified zeolite. Based on the above-mentioned analysis, 400 °C was found to be the optimal calcination temperature for AsH$_3$ adsorption.

3.2.4 The effects of the reaction temperature on AsH$_3$ adsorption. The reaction temperature was also closely investigated in this study. The low temperature of the system cannot provide sufficient heat to activate the gas molecules; thus, the gas and the active substances cannot be directly involved in the chemical reaction on the zeolite. All kinds of gases can be adsorbed *via* physical adsorption on any adsorbent. However, physical adsorption, which is produced only by weak van der Waals forces between the gas phase and solid phase, is usually reversible and without selectivity. The AsH$_3$ breakthroughs observed on the Cu/Hβ bed at 20, 40, 60, and 80 °C are illustrated in Fig. 10. Notably, it is found that the reaction temperature is one of the most critical factors that can affect the removal efficiency of AsH$_3$. As shown in Fig. 10, the AsH$_3$ removal efficiency was significantly enhanced upon increasing the reaction temperature. However, when the temperature reaches a certain point (60 °C), the effect of a further increase in the reaction temperature on the AsH$_3$ adsorption efficiency is no longer observed. Physical adsorption, chemical adsorption, and catalytic oxidation are expected to play a role during the removal process of AsH$_3$ on Cu/Hβ. Temperature has an influence on all the abovementioned mechanisms; a higher temperature promotes catalytic oxidation and chemical adsorption but definitively inhibits physical adsorption. From the experiments, it can be concluded that the optimal reaction temperature for Cu/Hβ is 60 °C, at which the AsH$_3$ adsorption capacity reaches 43.7 mg of AsH$_3$/(g of Cu/Hβ).

3.2.5 The effects of the oxygen content on AsH$_3$ adsorption. The effect of oxygen content on the AsH$_3$ breakthrough for Cu/Hβ at 60 °C is presented in Fig. 11, and the AsH$_3$ adsorption experiments have been conducted at an oxygen content maintained at 0%, 0.5%, 1.0%, 1.5%, and 2.0%. The oxygen content is another

important factor that influences the adsorption efficiency of AsH$_3$, and a supplement of trace oxygen can help reach a better removal efficiency. The increase in oxygen content can combine lattice oxygen with AsH$_3$ on the adsorbent surface, improve the mixture's total air speed, and avoid the influence of external diffusion. This makes the AsH$_3$ molecules overcome the resistance of diffusion and enter the pore channels of the modified zeolite. Thus, the AsH$_3$ molecules can fully contact the active substances in the pores, react with each other, and improve the adsorption efficiency. As illustrated in Fig. 11, the adsorption efficiency is significantly improved upon increasing the oxygen content, but no apparent efficiency increase is observed when the oxygen content is higher than 1.0%.
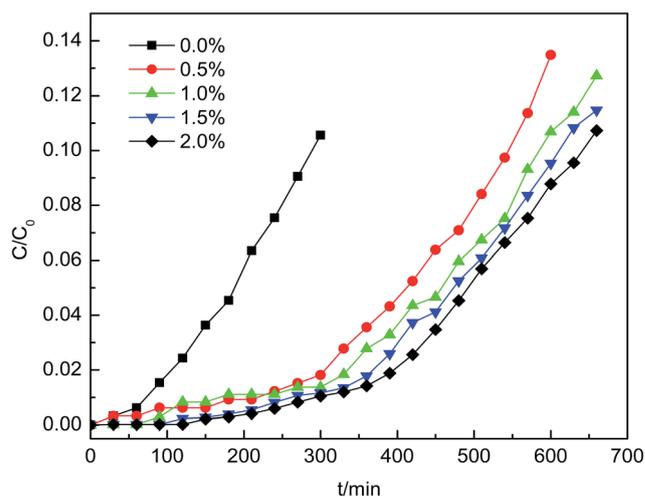

Fig. 11 The AsH$_3$ breakthrough curves obtained for a Cu/Hβ fixed bed at 60 °C as a function of the oxygen content (AsH$_3$ inlet concentration = 200 mg m^{-3}, impregnation concentration = 0.2 mol L^{-1} and calcination temperature = 400 °C).

3.3 Thermal regeneration

Heating the adsorbents and then blowing with a nitrogen flow were performed in the spent adsorbent regeneration experiments. The Cu/Hβ–AsH$_3$ sample was first reactivated for 4 h under hot air and washed with distilled water to a constant pH after cooling down to room temperature. The second step was to dry the sample at 110 °C for 5 h. Finally, the dried sample was heated at 300 °C for 3 h under N$_2$ at a flow rate of 30 mL min^{-1} in the tube furnace and then cooled down to room temperature. Fig. 12 shows the AsH$_3$ breakthrough behavior of Cu/Hβ, which has been used in the AsH$_3$ breakthrough test with subsequent thermal regeneration (the sample is referred to as Cu/Hβ-R1, Cu/Hβ-R2, and Cu/Hβ-R3). The generation efficiency of adsorbents and the regeneration time were the two key parameters used to investigate the adsorbent regeneration performance. When compared with that of fresh Cu/Hβ, the adsorption behaviors of the spent adsorbents (Cu/Hβ-R1) were similar and the breakthrough time remained as long as 430 min. However, Cu/Hβ-R2 and Cu/Hβ-R3 displayed a shorter breakthrough time than Cu/Hβ-R1. Despite the adsorption reaction being carried on for 290 min, the adsorption efficiency of Cu/Hβ-R3 for AsH$_3$ still remained above 95%. This result indicated that the regeneration thermal desorption was effective, and the Cu/Hβ zeolite adsorbent could be recycled at least two times with a slight loss in capacity.
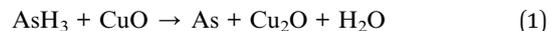
3.4 Identification of the AsH$_3$ adsorption mechanism

Considering all the characterization results, the Hβ zeolite is a highly efficient adsorption material. The addition of copper to the zeolite and the formation of a CuO active phase upon calcination at high temperatures allowed the removal of AsH$_3$ in an efficient manner.

Based on the XRD, XPS, and infrared spectroscopy analysis results, a reaction model for AsH$_3$ adsorption over the copper-exchanged zeolite adsorbent was proposed. The reaction involves (1) the reaction of adsorbed AsH$_3$ and CuO, and the generation of Cu$^+$, As, and oxygen vacancies; (2) O$_2$ activation on the oxygen vacancies and formation of surface activated oxygen or lattice oxygen; (3) the reaction of As and surface activated oxygen or lattice oxygen and the formation of As$_2$O$_5$; and (4) the newly generated Cu$^+$ and oxygen vacancies involved in the successive cycles.

Considering the abovementioned discussion, the AsH$_3$ adsorption process can be divided into the following steps:

$$AsH_3 + CuO \rightarrow As + Cu_2O + H_2O \qquad (1)$$

$$As + O_2 \rightarrow As_2O_5 \qquad (2)$$

$$Cu_2O + O_2 \rightarrow CuO \qquad (3)$$

A possible total chemical reaction formula on the zeolite surface was proposed as follows:

$$2AsH_3 + 4O_2 \rightarrow As_2O_5 + 3H_2O \qquad (4)$$
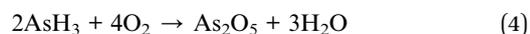
4. Conclusions

The Hβ zeolite loaded with metal salts has been prepared using an impregnation method and tested for AsH$_3$ removal. When compared with other adsorbents, the Cu/Hβ sample exhibited a significant improvement for AsH$_3$ adsorption with a breakthrough time of 390 min. In this study, we found that the best breakthrough capacity was 43.7 mg AsH$_3$/g Cu/Hβ adsorbent at 60 °C with 1.0% oxygen content on Cu/Hβ, which was prepared *via* calcination at 400 °C using an impregnation concentration of Cu(NO$_3$)$_2$ of 0.2 mol L^{-1}.

The Cu(NO$_3$)$_2$ impregnation likely results in the formation of surface functional groups, which significantly contribute to the pronounced increase in the AsH$_3$ adsorption capacity. The XRD and BET results revealed that a crystalline phase of CuO was formed on the zeolite surface and affected the specific surface area and pore structure. In addition, the XPS results showed that the products of AsH$_3$ adsorption were As$_2$O$_5$ species, which were accumulated on the zeolite surface and had a negative effect on the adsorption activity. It is feasible that the spent Cu/Hβ can be regenerated *via* thermal desorption, and the adsorbents can be recycled at least two times with a small amount of capacity loss.

Conflicts of interest

There are no conflicts to declare.

Acknowledgements

References

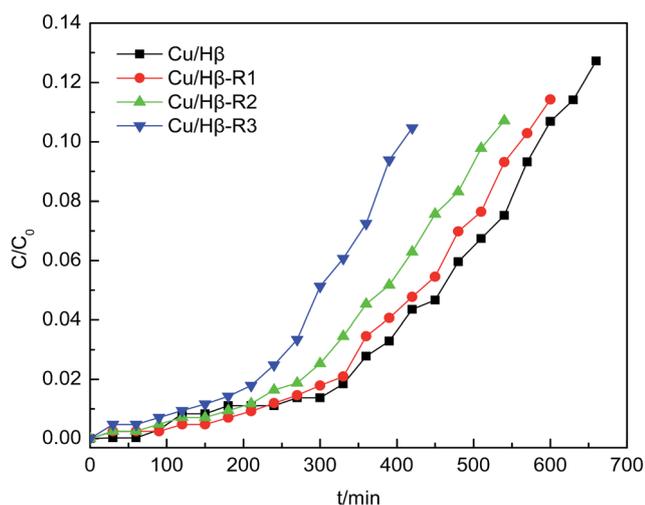1 T. A. Ivandini, D. Yamada, T. Watanabe, H. Matsuura, N. Nakano, A. Fujishima and Y. Einaga, Development of

Fig. 12 The AsH$_3$ breakthrough curves obtained for the fresh and regenerated Cu/Hβ adsorbent samples.

ampere metric arsine gas sensor using gold-modified diamond electrodes, *J. Electroanal. Chem.*, 2010, **645**, 58–63.

2 J. R. Bunt and F. B. Waanders, Trace element behavior in the Sasol–Lurgi MK IV FBDB gasifier. Part 1 – the volatile elements: Hg, As, Se, Cd and Pb, *Fuel*, 2008, **87**, 2374–2387.

3 M. Díaz-Somoano and M. R. Martínez-Tarazona, Trace element evaporation during coal gasification based on a thermodynamic equilibrium calculation approach, *Fuel*, 2003, **82**, 137–145.

4 S. Q. Liu, Y. T. Wang, Y. Li and J. Oakey, Thermodynamic equilibrium study of trace element transformation during underground coal gasification, *Fuel Process. Technol.*, 2006, **87**, 209–215.

5 J. P. Trembly, R. S. Gemmen and D. J. Bayless, The effect of coal syngas containing AsH$_3$ on the performance of SOFCs: investigations into the effect of operational temperature, current density and AsH$_3$ concentration, *J. Power Sources*, 2007, **171**, 818–825.

6 Z. H. Wang, M. Jiang, P. Ning and G. Xie, Thermodynamic modeling and gaseous pollution prediction of the yellow phosphorus production, *Ind. Eng. Chem. Res.*, 2011, **50**, 12194–12202.

7 M. Goldman and J. C. Dacre, *Lewisite: Its Chemistry, Toxicology, and Biological Effects*, Springer, New York, 1989.

8 S. M. Cohen, L. L. Arnold, M. Eldan, A. S. Lewis and B. D. Back, Methylated arsenicals: the implications of metabolism and carcinogenicity studies in rodents to human risk assessment, *Crit. Rev. Toxicol.*, 2006, **36**, 99–133.

9 J. K. Suh, N. Kang and J. B. Lee, Direct determination of arsine in gases by inductively coupled plasma-dynamic reaction cell-mass spectrometry, *Talanta*, 2009, **78**, 321–325.

10 R. Quinn, T. A. Dahl, B. W. Diamond and B. A. Toseland, Removal of arsine from synthesis gas using a copper on carbon adsorbent, *Ind. Eng. Chem. Res.*, 2006, **45**, 6272–6278.

11 R. Quinn and B. A. Toseland, Liquid-phase guard bed for removal of synthesis gas contaminants, *Ind. Eng. Chem. Res.*, 2008, **47**, 7027–7030.

12 E. C. Rupp, E. J. Granite and D. C. Stanko, Laboratory scale studies of Pd/γ-Al$_2$O$_3$ adsorbents for the removal of trace contaminants from coal-derived fuel gas at elevated temperatures, *Fuel*, 2013, **108**, 131–136.

13 C. X. Han, X. Y. Han, Y. Li, S. X. Liu and B. G. Zhang, Removal of arsine in PH$_3$ by Fe-based alloy, *Chin. J. Environ. Eng.*, 2010, **4**, 1601–1604.

14 C. J. Howard, R. A. Dagle, V. M. Lebarbier, J. E. Rainbolt, L. Y. Li and D. L. King, Progress toward biomass and coal-derived syngas warm cleanup: proof-of-concept process demonstration of multicontaminant removal for biomass application, *Ind. Eng. Chem. Res.*, 2013, **52**, 8125–8138.

15 M. Seredych, M. Merwe and T. J. Bandosz, Effects of surface chemistry on the reactive adsorption of hydrogen cyanide on activated carbons, *Carbon*, 2009, **47**, 2456–2465.

16 R. N. Nickolov and D. R. Mehandjiev, Comparative study on removal efficiency of impregnated carbons for hydrogen cyanide vapors in air depending on their phase composition and porous textures, *J. Colloid Interface Sci.*, 2004, **273**, 87–94.

17 P. A. Barnes, M. J. Chinn, E. A. Dawson and P. R. Norman, Preparation, characterisation and application of metal-doped carbons for hydrogen cyanide removal, *Adsorpt. Sci. Technol.*, 2002, **20**, 817–833.

18 P. W. Ye, Z. Q. Luan, K. Li, L. Q. Yu and J. C. Zhang, The use of a combination of activated carbon and nickel microfibers in the removal of hydrogen cyanide from air, *Carbon*, 2009, **47**, 1799–1805.

19 S. Poulston, E. J. Granite, H. W. Pennline, H. Hamilton and A. W. J. Smith, Palladium based adsorbents for high temperature arsine removal from fuel gas, *Fuel*, 2011, **90**, 3118–3121.

20 M. Jiang, Y. W. Bai, P. Ning, X. F. Huang, H. P. Liu and J. Q. Fu, Adsorption removal of arsine by modified activated carbon, *Adsorption*, 2015, **21**, 135–141.

21 M. J. Hudson, J. P. Knowles, P. J. F. Harris, D. B. Jackson, M. J. Chinn and J. L. Ward, The trapping and decomposition of toxic gases such as hydrogen cyanide using modified mesoporous silicates, *Microporous Mesoporous Mater.*, 2004, **75**, 121–128.

22 W. C. Li, H. Bai, J. N. Hu, S. N. Li and C. Chen, Metal loaded zeolite adsorbents for phosphine removal, *Ind. Eng. Chem. Res.*, 2008, **47**, 1501–1505.

23 X. Q. Wang, P. Ning, Y. Shi and M. Jiang, Adsorption of low concentration phosphine in yellow phosphorus off-gas by impregnated activated carbon, *J. Hazard. Mater.*, 2009, **171**, 588–593.

24 F. C. Wu, R. L. Tseng and C. C. Hu, Comparisons of pore properties and adsorption performance of KOH-activated and steam-activated carbons, *Microporous Mesoporous Mater.*, 2005, **80**, 95–106.

25 P. Ning, K. Li, H. H. Yi, X. L. Tang, J. H. Peng and D. He, Simultaneous catalytic hydrolysis of carbonyl sulfide and carbon disulfide over modified microwave coal-based active carbon catalysts at low temperature, *J. Phys. Chem. C*, 2012, **116**, 17055–17062.

26 K. S. W. Sing, D. H. Everett, R. A. W. Haul, L. Moscow, R. A. Pierotti, J. Rouquerol and T. Siemieniewska, Reporting physisorption data for gas/solid systems with special reference to the determination of surface area and porosity, *Pure Appl. Chem.*, 1985, **57**, 603–619.

27 K. Borgohain, J. B. Singh, M. V. R. Rao, T. Shripathi and S. Mahamuni, Quantum Size Effects in CuO Nanoparticles, *Phys. Rev. B*, 2000, **61**, 11093–11096.

28 Z. H. Yu, L. Zhou, Y. F. Huang, Z. G. Song and W. W. Qiu, Effects of a manganese oxide-modified biochar composite on adsorption of arsenic in red soil, *J. Environ. Manage.*, 2015, **163**, 155–162.

29 U. Zielke, K. Huttinger and W. Hoffman, Surface-oxidized carbon fibers: I. Surface structure and chemistry, *Carbon*, 1996, **34**, 983–988.

30 P. M. Alvarez, J. F. Garcia-Araya, F. J. Beltran, F. J. Masa and F. Medina, Ozonation of activated carbons: effect on the adsorption of selected phenolic compounds from aqueous solutions, *J. Colloid Interface Sci.*, 2005, **283**, 503–512.

31 P. Fanning and M. Vannice, A drifts study of the formation of surface groups on carbon by oxidation, *Carbon*, 1993, **31**, 721–730.

32 G. Z. Qu, N. Lu, J. Li, Y. Wu, G. F. Li and D. Li, Simultaneous pentachlorophenol decomposition and granular activated carbon regeneration assisted by dielectric barrier discharge plasma, *J. Hazard. Mater.*, 2009, **172**, 472–478.

33 S. Z. Zhao, H. H. Yi, X. L. Tang, D. J. Kang, H. Y. Wang, K. Li and K. J. Duan, Characterization of Zn–Ni–Fe hydrotalcite-derived oxides and their application in the hydrolysis of carbonyl sulfide, *Appl. Clay Sci.*, 2012, **56**, 84–89.

34 O. Shenderova, A. M. Panich, S. Moseenkov, S. C. Hens, V. Kuznetsov and H. M. Vieth, Hydroxylated detonation nanodiamond: FTIR, XPS, and NMR studies, *J. Phys. Chem. C*, 2011, **115**, 19005–19011.

35 E. Eren and B. Afsin, An investigation of Cu(II) adsorption by raw and acid-activated bentonite: a combined potentiometric, thermodynamic, XRD, IR, DTA study, *J. Hazard. Mater.*, 2008, **151**, 682–691.

36 Q. Zhao, S. L. Tian, L. X. Yan, Q. L. Zhang and P. Ning, Novel HCN sorbents based on layered double hydroxides: sorption mechanism and performance, *J. Hazard. Mater.*, 2015, **285**, 250–258.

37 M. R. Karagas, A. Gossai, B. Pierce and H. Ahsan, Drinking Water Arsenic Contamination, Skin Lesions, and Malignancies: A Systematic Review of the Global Evidence, *Curr. Environ. Health Rep.*, 2015, **2**(1), 52–68.